ACSNANO

www.acsnano.org

ARTICLE

Synergistic Enhancement of Fluorescence and Magnetic Resonance Signals Assisted by Albumin Aggregate for Dual-Modal Imaging

Lirong Wang,● Qing Wan,● Rongyuan Zhang, Bo Situ, Kaiyuan Ni, Jinhao Gao, Xing Feng, Pengfei Zhang, Zhiming Wang,* Anjun Qin,* and Ben Zhong Tang

Cite This: *ACS Nano* 2021, 15, 9924–9934

Read Online

ACCESS | Metrics & More | Article Recommendations | Supporting Information

ABSTRACT: **Dual-modal fluorescence and magnetic resonance imaging (FLI/MRI) is important for the early diagnosis of malignant tumors. However, facile and opportune strategies to synergistically enhance fluorescence intensity and magnetic resonance (MR) contrast have rarely been reported. Herein, we present a facile strategy using albumin aggregates (AAs) to synergistically enhance the fluorescence intensity by aggregation-induced emission (AIE) and MR contrast with prolonged rotational correlation time (τ_R) of Gd(III) chelates and the diffusion correlation time (τ_D) of surrounding water molecules. The amphiphilic dual-modal FLI/MRI probe of NGd was facilely loaded into albumin pockets and then formed AAs to generate a supramolecular structure of NGd-albumin aggregates (NGd-AAs), which show excellent biocompatibility and biosafety, and exhibit superior fluorescence quantum yield and r_1 over NGd with 6- and 8-fold enhancement, respectively. Moreover, compared with the clinical MRI contrast agent Gd-DOTA, r_1 of NGd-AAs showed a 17-fold enhancement. Therefore, NGd-AAs successfully elicited high-performance dual-modal FLI/MRI *in vitro* and *in vivo* and high contrast MR signals were observed in the liver and tumor after intravenous injection of NGd-AAs at a dosage of 6 μmol Gd(III)/kg body weight. This generic and feasible strategy successfully realized a synergistic effect for dual-modal FLI/MRI.**

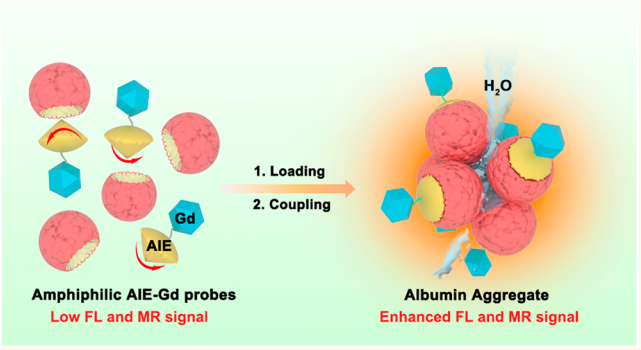

KEYWORDS: *albumin aggregate, fluorescence, magnetic resonance signal, aggregation-induced emission, synergistic enhancement*

INTRODUCTION

Cancer incidence and mortality are rapidly increasing and it is expected to rank as the leading cause of death worldwide.[1] To fight against cancer, it is particularly urgent and important to develop accurate diagnostic techniques to detect lesions as early as possible. Multimodal imaging plays an important role in the early and accurate diagnosis of malignant tumors.[2,3] Among the widely used imaging techniques, fluorescence imaging (FLI) shows high sensitivity but is limited by tissue-penetration of light for deep-seated tumors. In stark contrast, magnetic resonance imaging (MRI) stands out by virtue of nonionization, unlimited tissue-penetration depth, and high spatial resolution, but is hurdled by low sensitivity due to abundant background signal. Integrating FLI and MRI to complement each other with the creation of dual-modal FLI/MRI has aroused great interest among researchers in the development of dual-modal FLI/MRI probes.[4,5]

FLI/MRI dual-modal probes can be simply constructed by conjugating/coupling various fluorescent moieties with Gd chelates.[6−8] For MR contrast, Gd chelates mainly contribute to the T_1 contrast effect, and their contrast ability can be quantified by relaxivity (r_1),[9] which is positively associated with the rotational correlation time (τ_R) of the contrast agents and the diffusion correlation time (τ_D) of water molecules around the contrast agents.[10−14] Therefore, it is very important to ensure that Gd chelates contained in the FLI/MRI dual-modal probes can easily access water molecules under physiological conditions to enhance the contrast effect. However, the fluorescence

Received: February 9, 2021
Accepted: June 1, 2021
Published: June 7, 2021

https://doi.org/10.1021/acsnano.1c01251
ACS Nano 2021, 15, 9924–9934

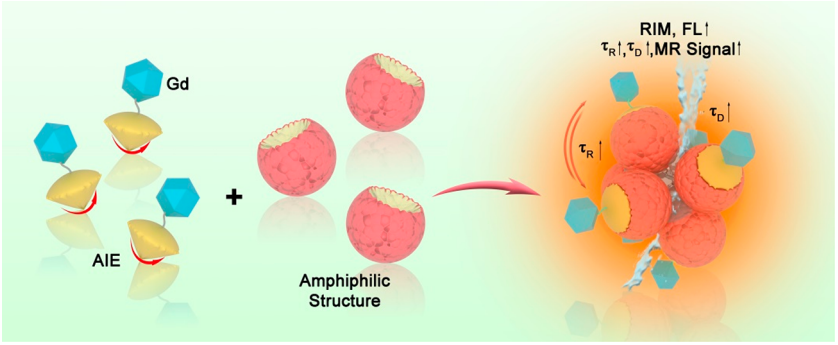

Figure 1. Schematic illustration of the amphiphilic structures loaded with AIE moiety-Gd molecules that generate supramolecular aggregates with enhanced fluorescence emission and improved MR signal.

intensity of FLI/MRI dual-modal probes is usually affected by a notorious aggregation-caused quenching effect under physiological conditions. Aggregation-induced emission (AIE) with restriction of intramolecular motion (RIM) working mechanism is a meaningful strategy to address this problem.[15−18] Combining Gd chelates with AIE moieties (AIE-Gd) into amphiphilic dual-modal probes would not only enhance the fluorescence intensity but also improve the relaxivity with prolonged τ_R.[8] Unfortunately, owing to the strong hydrophobicity of the AIE moieties, the Gd chelates are easily embedded inside the tightly packed aggregates and cannot get access to ambient water easily. Opposite strategies for constructing Gd chelates on the outside and AIE moiety on the inside need to be precisely designed, which is limited by the properties of the substrates and the preparation process, making them not universal and practical.[8,19] Therefore, to satisfy the constraint of intramolecular motion in a hydrophilic environment, we proposed that an amphiphilic structure with geometrically confined space would be ideal to load AIE-Gd dual-modal probes for this purpose. Owing to the hydrophobic interactions and steric hindrance, the intramolecular motion of the AIE moieties could be restricted to enhance the fluorescence of FLI. Meanwhile, compared with a single molecule, the larger size of nanoaggregates with longer τ_R would strongly improve the relaxivity for MRI. Furthermore, the geometrically confined structure of these nanoaggregates facilitates movement of water molecules in and out with a slow diffusion rate, that is, it prolongs τ_D of water molecules, which would further contribute to the improvement of relaxivity (Figure 1).

For amphiphilic structures, albumin is the best choice with incomparable advantages, such as biocompatibility and biodegradability.[20,21] Different albumin-based biomaterials with desired properties have been developed over the past few decades.[22,23] Due to its amphiphilic structure, albumin has been widely reported as a superb nanocarrier to either improve the relaxivity[24,25] or enhance the fluorescence intensity based on RIM of AIE moieties.[26,27] Therefore, we designed an amphiphilic FLI/MRI dual-modal probe of NGd by combining the AIE moiety and Gd-DOTA, which could closely bind to bovine serum albumin (BSA). Thereafter, we constructed NGd-Albumin aggregates (NGd-AAs) through desolvation and glutaraldehyde coupling BSA to load NGd. Compared with NGd, the fluorescence quantum yield and r_1 of NGd-AAs had a more than 6- and 8-fold improvement, respectively, and their r_1 was almost 17 times higher than that of the clinical contrast agent of Gd-DOTA. The phantom images demonstrated that NGd-AAs showed higher signal contrast than NGd at the same concentration. Moreover, the results of cell phantom imaging and confocal laser scanning microscopy (CLSM) verified that NGd-AAs were internalized more by Murine breast cancer 4T1 cells and had successfully achieved dual-mode FLI/MRI *in vitro*. Furthermore, *in vivo* T_1-weighted MR imaging indicated that NGd-AAs had a superior ability to contrast the liver and tumors at a dosage of 6 μmol Gd(III)/kg body weight. Thanks to the good biocompatibility of NGd-AAs, they have a higher enrichment at the tumor than NGd, which facilitated them for FLI. Moreover, a biodistribution study showed that NGd-AAs were mainly excreted by hepatobiliary metabolism, and laboratory tests confirmed that they had good biosafety *in vivo*. We propose that the "Albumin aggregate" structure would be an efficient strategy to achieve the synergistic enhancement of fluorescence intensity and MR contrast effect by combining the AIE mechanism and prolonging the τ_R of Gd chelates and τ_D of water molecules around Gd chelates.

RESULTS AND DISCUSSION

Synthesis and Characterization of NGd-AAs. The donor−acceptor (D−A) strategy was employed to construct the fluorescent moiety, in which dimethoxyl triphenylamine and 2*H*-naphtho[2,3-*d*] triazole core (NT) were used as the electron-donating and electron-accepting units, respectively. With the introduction of undecylic acid to the triazole part, Gd-DOTA was conjugated with the fluorophore to obtain the FLI/MRI dual-modal probe of NGd. The detailed synthesis and characterization of NGd are shown in the Figure 2a and Supporting Information (Supporting Information (SI) Scheme S1 and Figures S1−S6), respectively.

NGd shows an absorption maximum at 435 nm and a fluorescent peak at 570 nm in tetrahydrofuran (THF) (Figure 2b). NGd is AIE active. As shown in Figures 2c,d, its emission intensity decreased with the addition of water into dimethyl sulfoxide (DMSO) until water fraction (f_w) reached 20% because of the twisted intramolecular charge transfer process. On increasing f_w from 20 to 70%, the fluorescence intensity was gradually enhanced, but when f_w exceeded 70%, the fluorescence intensity decreased. This might be ascribed to the formation of aggregates with large sizes, which sink to the bottom and decrease the effective concentration of NGd in the detection beam zone.[28] This was also proved by the decrease in the relaxation rate of NGd in DMSO/water mixtures when f_w was higher than 50% (SI Figure S7). Notably, the introduction of Gd-DOTA into the AIE moiety did not affect its AIE property (SI Figure S8). Due to the amphiphilic characteristics of NGd, the critical micelle concentration of NGd was determined to be

https://doi.org/10.1021/acsnano.1c01251
ACS Nano 2021, 15, 9924−9934

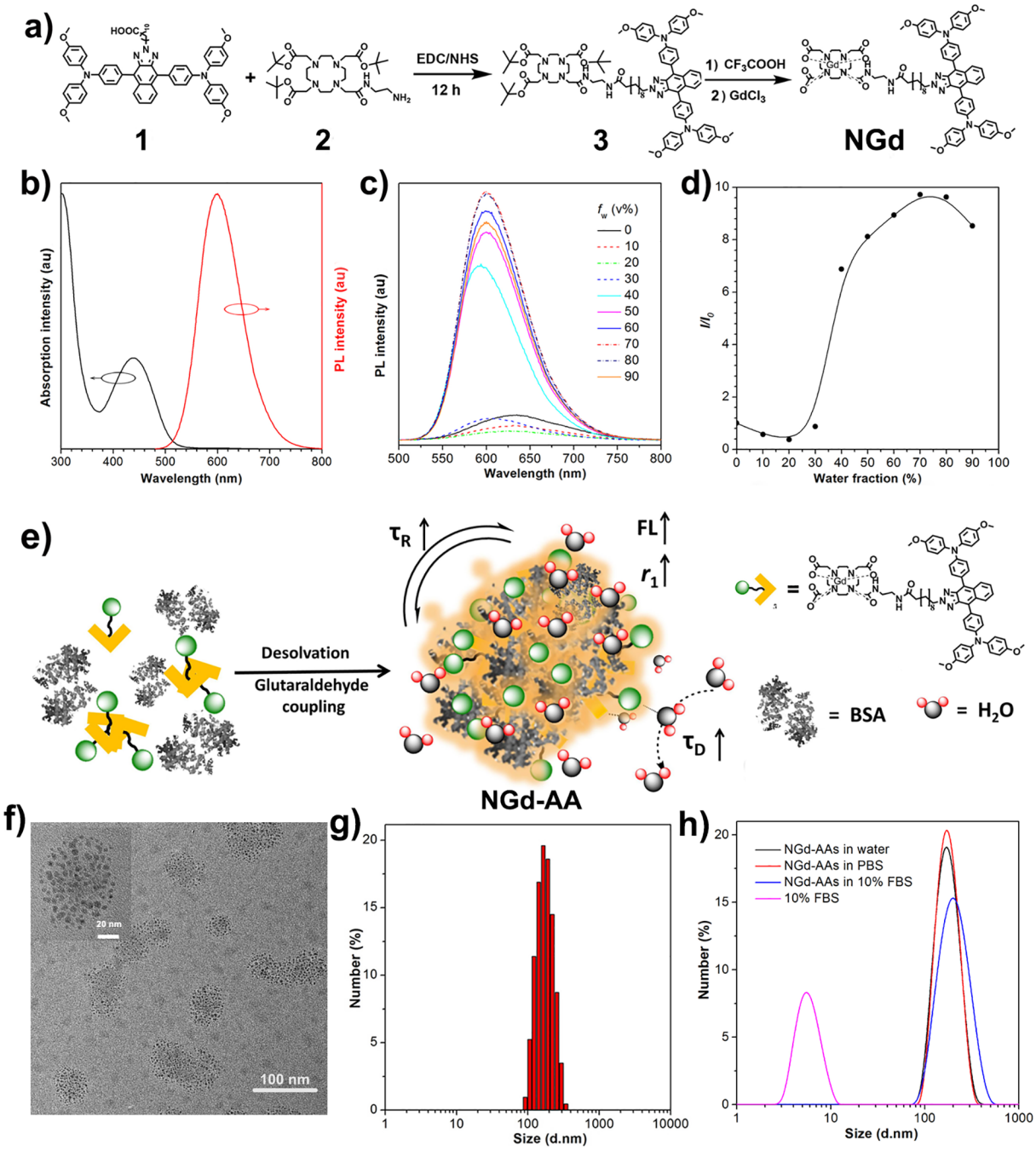

Figure 2. (a) Synthesis of NGd. Compounds 1 and 2 were condensed to produce the intermediate 3 followed by deprotection of the *tert*-butyl groups of 3 with trifluoroacetic acid (CF_3COOH) and coordination with $GdCl_3$. (b) Absorption and photoluminescence (PL) spectra of NGd in THF (10 μM). (c) PL spectra of NGd (10 μM) in DMSO/water mixtures with different water fractions (f_w). (d) Plot of the relative emission intensity of NGd versus water fraction. I_0 and I are the peak values of PL intensities of NGd (10 μM) in DMSO/water mixtures with different f_w. (e) Schematic illustration of the synthesis of NGd-Albumin aggregates (NGd-AAs) and the mechanism of synergistic FLI/MRI enhancement. (f) The morphology characterization of NGd-AAs measured by TEM. Inset: higher magnification of TEM image of NGd-AAs. (g) Hydrodynamic diameter of NGd-AAs in water measured by DLS. (h) DLS results of NGd-AAs in DI water, PBS, and 10% FBS, respectively, and 10% FBS alone.

25 μM (SI Figure S9) by using emission intensity. This reveals that NGd molecules are prone to form aggregates.

To ensure the interaction between NGd molecules and BSA, their binding affinity was estimated by proton relaxation enhancement (PRE)[29] and isothermal titration calorimetry (ITC). The result of PRE demonstrated a high affinity between NGd and BSA with a binding constant of 1.2×10^5 M^{-1} (SI Figure S10), which was almost at the same order of magnitude with the constant of 10.0×10^5 M^{-1} measured by ITC (SI Figure S11). In addition, as shown in SI Figure S10, the relaxation rate reached a maximum at a molar ratio of NGd/BSA = 2:1, which could guide our further synthesis of albumin aggregates. When NGd was added to the BSA aqueous solution, the NGd-BSA complexes formed aggregates. To stabilize the disbanded structure of aggregates of suitable size, desolvation and glutaraldehyde coupling were applied to synthesize NGd-AAs

https://doi.org/10.1021/acsnano.1c01251
ACS Nano 2021, 15, 9924−9934

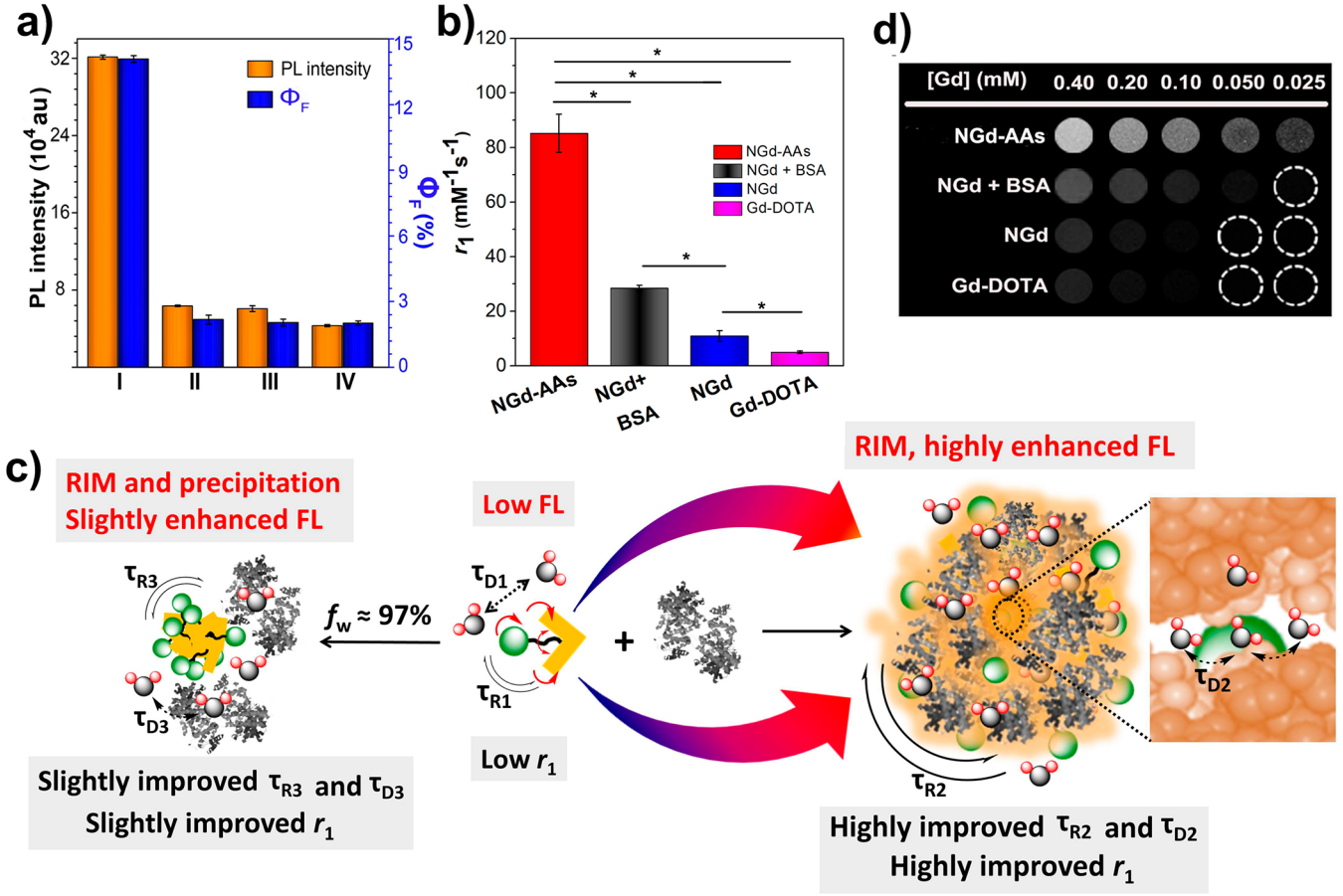

Figure 3. Exploration of fluorescence and relaxation effect. (a) PL intensity and fluorescence quantum yield (Φ_F) of (I) NGd-AAs and (II) NGd molecules in BSA solution (the molar ratio of NGd/BSA = 2:1), (III) in water, and (IV) in DMSO, respectively. (b) T_1 relaxivities of NGd-AAs, NGd in BSA aqueous solution (the molar ratio of NGd/BSA = 2:1), NGd in water, and Gd-DOTA at 0.5 T, respectively. Data are expressed as means ± SD ($n = 3$). *$P < 0.001$. (c) Illustration of the mechanism of simultaneous enhancement of fluorescence and relaxivity. τ_{R1}, τ_{R2}, and τ_{R3} refer to rotational correlation time of NGd molecules, NGd-AAs, and NGd aggregates in BSA aqueous solution, respectively; τ_{D1},τ_{D2}, and τ_{D3} are the diffusion correlation time of water molecules around them, respectively. (d) Phantom images of NGd-AAs, NGd in BSA aqueous solution, NGd in water, and Gd-DOTA at different Gd(III) concentrations, respectively.

with an initial feed molar ratio of NGd/BSA = 2:1 (Figure 2e). The encapsulation efficiency of NGd was deduced to be *ca.* 35%, which was mainly attributed to the fact that parts of NGd molecules were prone to form aggregates, partially hindering the interaction of NGd molecules with BSA. To characterize the morphology of NGd-AAs, transmission electron microscopy (TEM) and dynamic light scattering (DLS) were employed. As shown in Figure 2f, NGd-AAs were irregular aggregates with the size of ~110 nm, which were similar to the result of ~178 nm measured by DLS (Figure 2g). Moreover, at higher magnification, it was observed that NGd-AAs were composed of many small BSA nanoparticles with size of ~6 nm and the distance of them was 2−3 nm (Figure 2f). The results of molecular docking suggested that the aromatic AIE moieties of NGd were inserted in the pockets of BSA, however the long chain linked with Gd-DOTA with the spatial distance of about 2.1 nm was free (SI Figure S12). This could be the main reason to the separation of each BSA nanoparticles with distance of 2−3 nm. In addition, NGd-AAs were stable in deionized (DI) water, phosphate buffer solution (PBS), and fetal bovine serum (FBS) (Figure 2h), indicative of their high stability in physiological environments, and feasibility for biological applications.

Synergetic Enhancement of Fluorescence and MR Signals by NGd-AAs in Solution. To check whether the albumin aggregates could enhance the fluorescence intensity, the optical properties of NGd-AAs were explored. As shown in Figure 3a and SI Figure S13a, the fluorescence intensity of NGd-AAs is 7 and 5 times higher than that of NGd in DMSO and water, respectively. The fluorescence quantum yield (Φ_F) of NGd-AAs is almost 6 times higher than that of NGd in water or BSA aqueous solution, and more than 3 times higher than that of NGd in DMSO (Figure 3a and SI Table S1). The significantly enhanced fluorescence intensity and Φ_F of NGd-AAs could be attributed to the RIM of NGd by inserting into BSA aggregates (Figure 3c). Meanwhile, the fluorescence intensities of NGd in the DMSO/water mixture with f_w of 97% and DMSO were almost at the same level, but much lower than that of NGd in the DMSO/water mixture with f_w of 70% (SI Figure S13b). The reason might be that when f_w in the solvent mixture is larger than 70%, the aggregate sediments of NGd become larger and more in number, thereby decreasing the effective detection concentration, leading to a plateau in fluorescence intensity improvement. Because the aggregation of NGd hindered them from interacting effectively with BSA, the fluorescence intensity was not enhanced even after the addition of BSA (Figure 3a,c, and SI Figure S13). Furthermore, the emission peak had a significant blue shift for NGd-AAs compared with that of NGd in DMSO (SI Figure S13a), which was attributed to the noncovalent

https://doi.org/10.1021/acsnano.1c01251
ACS Nano 2021, 15, 9924−9934

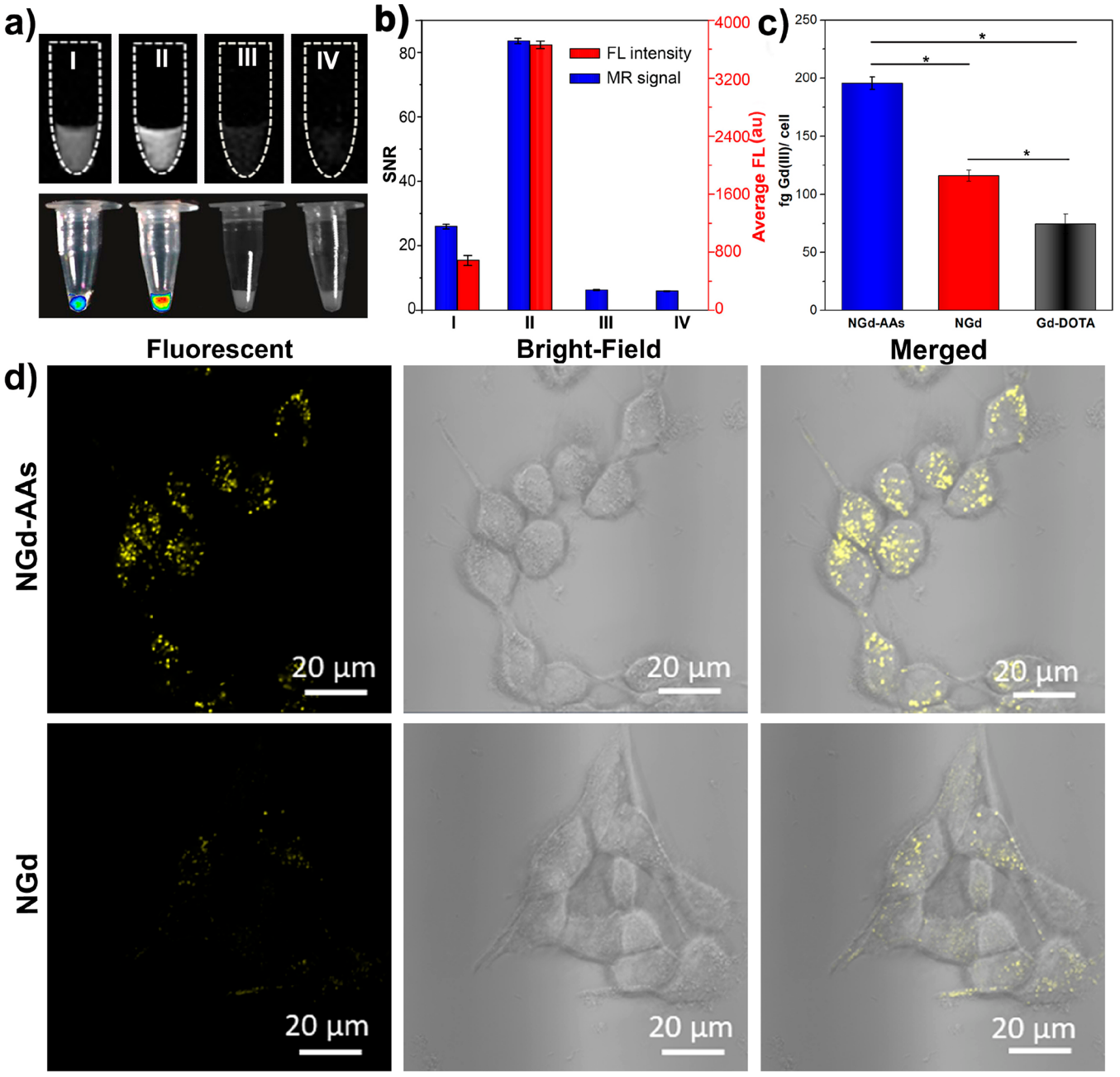

Figure 4. ***In vitro*** **dual-modal FLI/MRI of NGd-AAs. (a)** T_1**-weighted MRI (up) and fluorescence (down) images of cell pellets. (b) Comparison of signal-to-noise ratio (SNR) of** T_1**-weighted images (0.5 T, blue) and the average FL intensity (red) of cell pellets in panel (a). I, II, III, and IV refer to Murine breast cancer 4T1 cells incubated with NGd, NGd-AAs, Gd-DOTA, and PBS, respectively. (c) Quantification of cellular uptake of NGd-AAs, NGd, and Gd-DOTA, respectively. Data are expressed as means ± SD (**n **= 3). *P **< 0.001 (d) CLSM images of murine breast cancer 4T1 cells incubated with NGd-AAs and NGd. Scale bar: 20** μ**m, [NGd-AAs] = [NGd] = 10** μ**M.**

binding between NGd and BSA through hydrophobic interactions and ion pairing between the cationic groups of the gadolinium complex and amino acid residues.[27] Surprisingly, the fluorescence intensity of NGd-AAs was slightly weaker than that of NGd in the DMSO/water mixture with an f_w of 70% (SI Figure S13b). This result indicated that the packing of NGd-AAs was not as tight as that of NGd aggregates in water.

The slackened structure of NGd-AAs could generate geometrically confined effects for permitting the water molecules in and out slowly, thus might prolong τ_D of the water molecules, which is beneficial to the improvement of the MR contrast effect. Thus, the MR contrast effect of NGd-AAs was evaluated and compared with NGd molecules in water or BSA aqueous solution, and the clinical contrast agent of Gd-DOTA (Figure 3b and SI Figure S14a). The r_1 of NGd-AAs was deduced to be 85.1 ± 7.0 mM^{-1} s^{-1} at 0.5 T, which is 17 times and nearly 8 times higher than that of Gd-DOTA (4.9 ± 0.5 mM^{-1} s^{-1}) and NGd in aqueous solution (10.9 ± 1.2 mM^{-1} s^{-1}), respectively. This result verified that the strategy of the albumin aggregates could largely improve the relaxivity of contrast agents. Such a high relaxivity can be ascribed to the elongated τ_{R2} of large nanoparticles and τ_{D2} of water molecules trapped in the interstices of BSA aggregates ($\tau_{R1} < \tau_{R2}$ and $\tau_{D1} < \tau_{D2}$, Figure 3c).

https://doi.org/10.1021/acsnano.1c01251
ACS Nano 2021, 15, 9924−9934

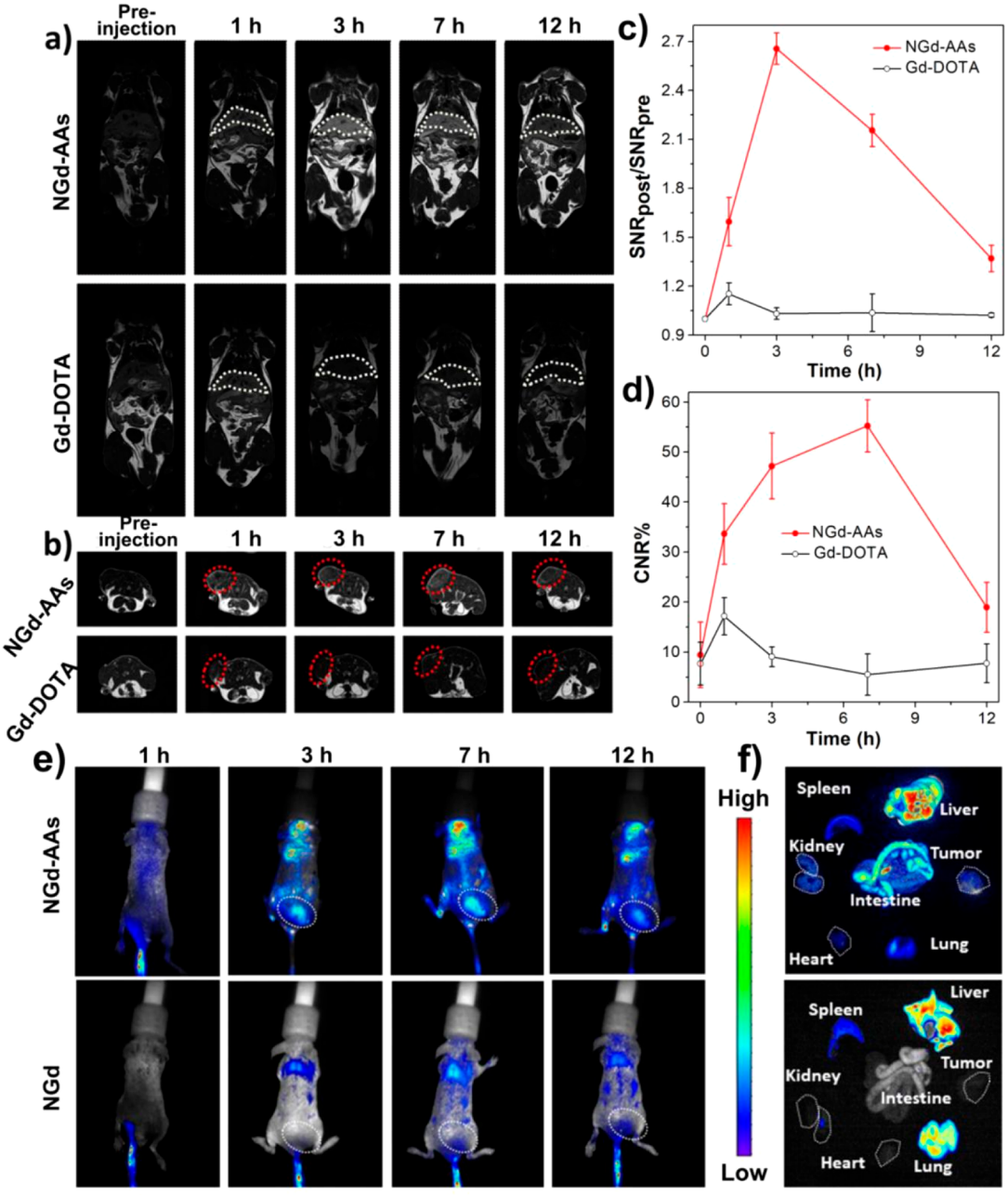

Figure 5. Dual-modal *in vivo* MRI and FLI.(a-d) T_1-weighted MRI and analysis of mice after intravenous injection of NGd-AAs or Gd-DOTA. (a) MRI of the liver with the dosage of 6 μM Gd(III)/kg body weight before and after intravenous injection at 1, 3, 7, and 12 h, respectively. The white dotted lines refer to the liver. (b) MRI of tumors before and after intravenous injection of NGd-AAs (up) and Gd-DOTA (down) at 1, 3, 7, and 12 h, respectively. The red dotted circles indicate the tumors. (c) Quantitative analysis of signal changes (SNR ratio) in liver versus treating time. (d) Contrast-to-noise ratios (CNR) of tumor and tissue contrast before and at 1, 3, 7, and 12 h after injection of the probes, respectively. CNR = $|SNR_{tumor} - SNR_{muscle}/SNR_{muscle}$. (e) FLI *in vivo* after intravenous injection of NGd-AAs or NGd at 1, 3, 7, 12 h. The white dotted lines refer to the tumors. (f) *Ex vivo* fluorescence images of main tissues (heart, liver, spleen, lung, kidney, and intestine) and tumors from mice at 12 h postinjection.

In addition, the relaxivity of NGd in aqueous solution was higher than that of Gd-DOTA owing to the high molecular weight of NGd and its aggregate state in water.[8] Furthermore, we dispersed NGd into the BSA aqueous solution at a molar ratio of 2:1, at which the relaxivity increased to 28.4 ± 1.0 mM^{-1} s^{-1}, which is 2 times higher than that of NGd in water. However, the value is still 3 times lower than that of NGd-AAs (Figure 3b and SI Figure S14a). This result could be attributed to the weak interaction of NGd aggregates (slightly elongated τ_{R3}) with BSA and the slight prolongation of τ_{D3} of water molecules by the "water-blocking" function of albumin ($\tau_{R1} < \tau_{R3} < \tau_{R2}$ and $\tau_{D1} < \tau_{D3} < \tau_{D2}$, Figure 3c). Furthermore, the phantom images of these four groups also proved that NGd-AAs had the high signal contrast compared with three other circumstances at the same Gd(III) concentrations (Figure 3d and SI Figure S14b).

From the phantom images, it was seen that NGd-AAs at a low Gd(III) concentration (0.025 mM) could reach the same contrast effect of Gd-DOTA at a 16-fold higher concentration (0.4 mM) (SI Figure S14b), which indicated that a lower dose could generate a satisfactory effect for NGd-AAs. Thus, the

https://doi.org/10.1021/acsnano.1c01251
ACS Nano 2021, 15, 9924−9934

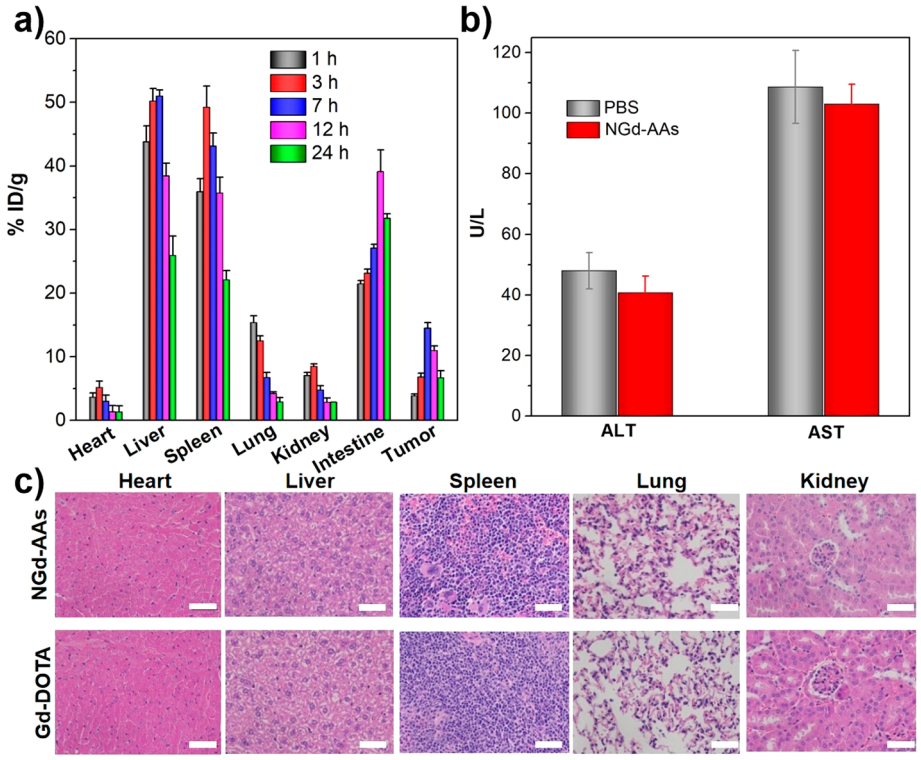

Figure 6. Biodistribution and biosafety assessment. (a) Biodistribution of NGd-AAs at 1, 3, 7, 12, and 24 h after injection in 4T1 tumor-bearing mice evaluated by ICP-MS (n = 3). (b) Serological test results of mice injected with NGd-AAs (30 μmol Gd(III)/kg body weight), PBS was as the control (n = 3). (c) H&E stained tissue sections from mice after intravenous injection of NGd-AAs (30 μmol Gd(III)/kg body weight) for one month, and PBS was used as a control. Scale bar: 50 μm for all images.

results of relaxivity and T_1-weighted images illustrate that these albumin aggregates loaded with NGd can also significantly improve the MR contrast effect. Combined with the enhanced fluorescence intensity, NGd-AAs would have great potential as a high-performance FLI/MRI dual-modal probe for *in vitro* imaging.

***In Vitro* Dual-Modal FLI/MRI of NGd-AAs.** We explored the dual-modal FLI/MRI of NGd-AAs *in vitro*. T_1-weighted MR images of Murine breast cancer 4T1 cells incubated with NGd-AAs, NGd, and Gd-DOTA with the same Gd(III) concentration of 100 μM were acquired. As shown in Figure 4a,b, the cells treated with NGd-AAs exhibited the strongest positive contrast signal among the NGd, Gd-DOTA, and PBS groups. Meanwhile, the fluorescence intensity of cells incubated with NGd-AAs was brighter than that with NGd. Because Gd-DOTA and PBS are nonemissive, no fluorescence signal was found in the cells treated with them. These results indicated that NGd-AAs could realize *in vitro* dual-modal FLI/MRI.

To quantify the amount of these probes per cell, inductively coupled plasma mass spectroscopy (ICP-MS) was employed (Figure 4c). The cellular uptake of NGd-AAs, NGd, and Gd-DOTA was about 195.6 ± 5.3, 116.1 ± 4.8, 74.5 ± 8.5 fg Gd(III)/cell, respectively. Furthermore, CLSM was employed to observe the intracellular accumulation of NGd-AAs and NGd. The results indicated that NGd-AAs were taken up more than NGd by 4T1 cells (Figure 4d). These results could be attributed to the gp60 albumin receptor distributed on cell surfaces, which can bind albumins to induce clustering of gp60-albumin and association with caveolin-1 and further complete the transcytosis process.[21] Moreover, 3-(4,5-dimerthylthiazol-2-yl)-2,5-diphenyltetrazolium bromide (MTT) assay showed that 4T1 cells had 100% viability after incubation with NGd-AAs for 24 h even at a Gd(III) concentration of 100 μM, while only 70% viability was obtained when incubated with NGd (SI Figure S15). These results suggest that NGd-AAs have better biocompatibility than NGd.

Dual-Modal FLI/MRI *In Vivo* of NGd-AAs. Considering the results of T_1-weighted contrast ability in the solution state, NGd-AAs were intravenously injected into 4T1 tumor containing mice with a low dose of 6 μmol Gd(III)/kg body weight for *in vivo* imaging. The T_1-weighted contrast capability of NGd-AAs in the liver and tumors of tumor containing mice was explored. The clinical contrast agent Gd-DOTA was used for comparison. T_1-weighted images at different interval were collected on a 1 T MRI scanner. As shown in Figure 5a, compared with preinjection, a high contrast signal in the liver can be easily seen over time, with a peak at 3 h postinjection, and the signal weakened at 12 h postinjection. For the control group with the same Gd(III) content, a faintly contrast signal was observed at 1 h postinjection and disappeared quickly owing to the rapid renal clearance and weak contrast effect of Gd-DOTA. Subsequently, we analyzed the contrast capability of NGd-AAs in the tumor region. As illustrated in Figure 5b, the positive signals of the tumor became more obvious than the preinjection signals and peaked at 7 h after injection. In contrast, there were few positive signals at different interval after injection of Gd-DOTA apart from the inferior bright signal at 1 h after injection.

In addition, we also used the values of SNR_{post}/SNR_{pre}[30,31] and contrast-to-noise ratios (CNR)[7,32] to quantitatively evaluate the change in enhanced contrast in the liver and tumors. In the liver, the SNR_{post}/SNR_{pre} values of T_1-weighted images were deduced to be 1.6 ± 0.2, 2.7 ± 0.1, 2.1 ± 0.1, 1.4 ± 0.1, at 1, 3, 7, and 12 h after administration of NGd-AAs, respectively (Figure 5c). Moreover, the peak signal at 3 h after injection was ~2.7-

https://doi.org/10.1021/acsnano.1c01251
ACS Nano 2021, 15, 9924−9934

fold higher than that of the preinjection. In contrast, the SNR_{post}/SNR_{pre} value of the control group showed a peak of 1.2 ± 0.1 at 1 h after injection, which was more than 2 times lower than that 3 h after injection of the NGd-AAs group. The highest CNR for tumors of NGd-AAs at 7 h after injection was ∼56%, which was almost 6 times and more than 3 times higher than that of prescan (∼9%) and the control group at 1 h after injection (∼17%), respectively (Figure 5d). These results suggest that NGd-AAs hold potential for T_1-weighted tumor imaging because of their large size, which could accumulate and retain them in the tumors owing to the enhanced permeability and retention effect.[33,34]

Then we tried to explore the FLI capability of NGd-AAs or NGd in the tumors. As shown in Figure 5e, the signal peaked at 7 h after injection of NGd-AAs and weakened over time, which was consistent with results of MRI in tumors (Figures 5b,d). As comparison, no signal was found at the tumor site for NGd groups. At 12 h after injection of NGd-AAs or NGd, heart, liver, spleen, lung, kidney, intestine, and tumor were collected for *ex vivo* FLI. As Figure 5f shows, for the NGd-AAs group, the liver exhibited the strongest fluorescence signal followed by intestine. While for NGd group, the strongest fluorescence signal belonged to the liver and lung, which could be attributed that NGd molecules with poor biocompatibility aggregated to oversized particles in the blood and blocked in the lung and liver.

Biodistribution and biosafety of NGd-AAs. The biodistribution of NGd-AAs in 4T1 tumor containing mice was explored at different intervals with a high dose of 30 μmol Gd(III)/kg body weight. To quantitatively assess the biodistribution of NGd-AAs, the heart, liver, spleen, lung, kidney, intestine, and tumors were collected and analyzed for Gd(III) content by ICP-MS. Unlike the *ex vivo* fluorescence signals, NGd-AAs showed the highest accumulation in the spleen, liver, and intestine, followed by the tumors, lung, and kidney (Figure 6a). The high accumulation of NGd-AAs in the spleen and liver could be attributed to the reticuloendothelial system (RES),[35] whereas enrichment in the intestine likely signifies the clearance of nanoparticles. Surprisingly, with similarly high contents of NGd-AAs in the spleen and liver at 12 h after injection (Figure 6a), weak fluorescent signal was observed in the spleen, but a strong fluorescent signal was detected in the liver (Figure 5f). This could be ascribed to the disparities in light absorption and scattering between the liver and spleen.[7,36] Uptake by tumors indicates that the large size of NGd-AAs extends their residence time in the body, which is conducive to the enhanced permeability and retention effect. All organs showed significantly decreased Gd(III) content after 12 h, further suggestive of the clearance of NGd-AAs. These data confirm that NGd-AAs are mainly taken up by RES and eliminated over time, probably by hepatobiliary metabolism.[37]

To evaluate long-term biosafety of NGd-AAs, serological and histological examinations were carried out. NGd-AAs were injected into healthy nude mice via the tail vein at a dosage of 30 μmol Gd(III)/kg body weight. For comparison, PBS buffer with the same volume was used under the same experimental conditions. After one month, all mice were sacrificed and dissected to collect the blood and main organs. Alanine aminotransferase (ALT) and aspartate aminotransferase (AST) are typical serum biochemical indices. As shown in Figure 6b, these two indices of mice treated with NGd-AAs were at a similar level to those of the PBS group, suggesting that NGd-AAs do not affect liver function. Moreover, hematoxylin and eosin (H&E) stained images showed no significant inflammation or cell necrosis in the main organs (Figure 6c), indicating that NGd-AAs have good biosafety.

CONCLUSION

A facile and straightforward strategy to synergistically enhance Φ_F and r_1 by an albumin aggregated dual-modal FLI/MRI probe of NGd-AAs was presented. This probe possesses good biocompatibility and AIE activity owing to the combination of RIM and prolonging the τ_R of Gd(III) chelates and τ_D of surrounding water molecules. Compared with NGd and the clinical contrast agent Gd-DOTA, NGd-AAs exhibited improvement in both fluorescence and T_1-weighted contrast, which endowed a high-performance dual-modal FLI/MRI *in vitro* and *in vivo*. This albumin-aggregate strategy realized a "1 + 1 > 2" effect for dual-modal FLI/MRI, which might be of valuable reference for researchers to develop biocompatible near-infrared (NIR) or NIR-II FLI/MRI dual-modal probes for accurate diagnosis and surgical navigation.

METHODS AND EXPERIMENTAL

Equipment and Methods. ^1H and ^{13}C NMR spectra were measured on a Bruker AV 500 spectrometer. High resolution mass spectra (HRMS) were recorded on an Acquity UPLC/XEVO G2-XS QTOF operating in MALDI-TOF mode. UV−vis absorption spectra were measured on a Shimadzu UV-2600 spectrophotometer. Photoluminescence spectra were recorded on a Horiba Fluoromax-4 spectrofluorometer. Photoluminescence (PL) quantum yields were measured using a Hamamatsu absolute PL quantum yield spectrometer C11347 Quantaurus QY. Confocal laser scanning microscope (CLSM) characterization was conducted with a Zeiss LSM 710 (Germany) confocal laser scanning biological microscope. The absorbance for MTT analysis was recorded on a Thermo Fisher microplate reader (USA) at a wavelength of 490 nm. The element analysis of Gd was also carried out by inductively coupled plasma mass spectroscopy (ICP-MS). The morphology and structure of NGd-AAs with phosphotungstic acid staining (1 wt %) were characterized by transmission electron microscopy (TEM) using a JEOL JEM-2100 transmission electron microscope. The dynamic light scattering (DLS) measurements were performed on a Malvern Zetasizer nano ZS instrument. The T_1 relaxation time measurements were performed on 0.5 T NMI20-Analyst NMR Analyzing & imaging system (Niumag Corporation, Shanghai, China), *in vivo* MR imaging was performed on a 1 T MRI System (Aspect M3, Israel). *In vivo* and *ex vivo* fluorescence imaging was carried out on Vital River Laboratory Animal Technology Co. Ltd. (Beijing, China).

Synthesis of Intermediate 4. The intermediate **4** was prepared by the bromination reaction according to previous literature.[38] A mixture of 1.7 mL of bromine (10.4 g, 43 mmol) and 50 mL of glacial acetic acid was gradually added into 70 mL of glacial acetic acid solution containing 2,3-dihydronaphthalene-2,3-diamine (NA) (2.5 g, 16 mmol), and then the solution was stirred at room temperature for 4 h. The deionized water was added into solution, and the precipitate was filtered off and washed with glacial acetic acid and water. The brown powder was obtained after drying (3.8 g, 81%).

Synthesis of Intermediate 5. The intermediate **5** was synthesized according to previous literature.[39] $NaNO_2$ aqueous solution (3.0 g, 33.0 mmol, 15 mL) was added dropwise to 30 mL of glacial acetic acid containing compound **4** (3.16 g, 10 mmol). After vigorous stirring for 30 min at room temperature, the precipitate was filtered off and washed with water to obtain brown powder. The crude product was directly used without further purification. The obtained brown powder (2.5 g, 7.6 mmol) was dissolved in dry DMF (30 mL) and NaOH (11.4 mmol, 456 mg) was added with vigorous stirring within 1 h. 11-Bromoundecanoic acid (4.1 g, 15.2 mmol) in DMF (20 mL) was added dropwise and the solution was stirred at room temperature for 24 h. Afterward, the solution was adjusted to faintly acid by dilute hydrochloric acid. Then, the solution was extracted with DCM/water

https://doi.org/10.1021/acsnano.1c01251
ACS Nano 2021, 15, 9924−9934

to remove DMF, the organic layer was dried over anhydride $MgSO_4$. After filtration and solvent evaporation, the crude product was purified by column chromatography using ethyl acetate/petroleum ether mixture as eluent to afford orange powder (2.8 g, 73%). ^{1}H NMR (DMSO-d_6, 500 MHz): δ 11.88 (s, 1H), 8.33 (m, 2H), 7.70 (m, 2H), 4.91 (t, 2H), 2.17 (m, 4H), 1.32−1.20 (m, 14 H). ^{13}C NMR (DMSO-d_6, 125 MHz): δ 174.9 142.4, 130.9, 128.1, 126.9, 108.5, 58.1, 34.1, 29.8, 29.2, 29.1, 28.9, 28.7, 26.3, 24.9. HRMS calculated for $C_{21}H_{26}Br_2N_3O_2$ $[M + H]^+$ m/z: 510.0392, found: 510.0387.

Synthesis of Compound 1. The compound **1** was synthesized by Suzuki coupling reaction. The mixture of [4-(bis(4-methoxyphenyl)-amino)phenyl]boronic acid (2.1 g, 6 mmol), intermediate **5** (1.53 g, 3 mmol) and $Pd(PPh_3)_4$ (116 mg, 0.1 mmol) were dissolved in 20 mL toluene and 12 mL K_2CO_3 (2 M) aqueous solution. Then, the mixture was refluxed under nitrogen for 24 h. After solvent evaporation, the crude product was purified by column chromatography using ethyl acetate/petroleum ether mixture as eluent to afford orange powder (1.7 g, 89%). ^{1}H NMR (DMSO-d_6, 500 MHz): δ 8.04 (d, 2H), 7.45 (d, 2H), 7.35 (d, 2H), 7.19 (d, 2H), 6.96 (d, 2H), 8.92 (d, 2H), 4.80 (t, 2H), 3.76 (s, 12 H), 1.98 (t, 2H), 1.87 (t, 2H), 1.26−1.15 (m, 14H). ^{13}C NMR (DMSO-d_6, 125 MHz): δ 174.9, 156.5, 148.3, 141.8, 140.3, 133.6, 132.8, 132.5, 132.3, 132.0, 131.9, 129.2, 127.8, 118.3, 115.5, 55.6, 34.1, 30.1, 29.2, 28.9, 26.4, 24.9. HRMS calculated for $C_{61}H_{62}N_5O_6$ $[M + H]^+$ m/z: 960.4700, found: 960.4717.

Synthesis of Compound 3 (N-DO3AtBu). Compound **1** (100 mg, 0.1 mmol), 1-(3-(dimethylamino)propyl)-3-ethylcarbodiimide hydrochloride (EDC) (28.7 mg, 0.15 mmol), *N*-hydroxysuccinimide (NHS) (17.3 mg, 0.15 mmol) were dissolved in dry DMF (10 mL) and stirring at room temperature for 1 h. The DMF solution (2 mL) of compound **2** [tri*tert*-butyl 2,2′,2″-(10-(2-((2-aminoethyl)amino)-2-oxoethyl)-1,4,7,10-tertraazacyclododecane-1,4,7-triyl)triacetate, 67.5 mg, 0.11 mmol], which was synthesized according to the previous procedures,[13] was added and the mixture was stirred at 50 °C for 10 h. Afterward, the solution was extracted with DCM/water, the organic layer was dried over anhydride $MgSO_4$. After filtration and solvent evaporation, the crude product was purified by column chromatography using methanol/DCM mixture as eluent to afford light-yellow powder compound **3** (99.5 mg, 64%). ^{1}H NMR (500 MHz, CD_2Cl_2): δ 8.14 (dd, 2H), 7.49 (d, 4H), 7.30 (dd, 2H), 7.21 (d, 8H), 7.07 (d, 4H), 6.91 (d, 8H), 4.80 (t, 2H), 3.81 (s, 12H), 3.34−3.19 (m, 4H), 2.83−2.08 (m, 26H), 1.84 (s, 2H), 1.71−0.96 (m, 41H). ^{13}C NMR (125 MHz, CD_2Cl_2): δ 177.82, 177.57, 175.02, 172.94, 170.64, 157.45, 149.82, 143.82, 141.63, 133.36, 131.33, 129.18, 128.42, 128.04, 127.87, 127.72, 125.63, 121.71, 120.37, 116.12, 91.90, 56.78, 54.75, 45.25, 43.64, 39.49, 37.49, 36.54, 35.73, 33.21, 32.45, 31.67, 31.01, 30.96, 30.86, 30.70, 30.59, 30.44, 30.36, 29.98, 29.24, 27.95, 26.24, 24.01, 15.93, 15.20. HRMS calculated for $C_{91}H_{118}N_{11}O_{12}$ $[M + H]^+$ m/z: 1556.8961, found: 1556.8981.

Synthesis of NGd. Compound **3** (90 mg, 0.06 mmol) was dissolved in 3 mL trifluoroacetate acid (TFA) at room temperature for deprotection. After stirring for 6 h, excess TFA was removed by rotary evaporation. And then, the resultant brown oily product was dissolved in methanol, and the pH of the solution was adjusted to 5−6 with dilute sodium hydroxide solution. Anhydrous gadolinium chloride (24 mg, 0.09 mmol) was dissolved into 3 mL methanol, and added dropwise into the above brown solution. After reaction overnight at 60 °C, the methanol was removed by evaporation. The crude product was redissolved in DCM, and the excess gadolinium ions were washed off with water to obtain the brown solid product (92.5 mg, 90%). HRMS (m/z) calculated for $C_{79}H_{91}GdN_{11}O_{12}$ $[M + H]^+$ m/z: 1542.6011, found: 1542.6017.

Preparation of NGd-AAs. NGd molecules were dissolved in DMSO at a Gd(III) concentration of 16.7 mM and kept in 4 °C refrigerator. NGd-AAs were prepared by desolvation followed by glutaraldehyde coupling.[13,40] NGd (181.4 μL) was diluted with 20 mL THF and dropwise added into 50 mL of BSA (~20 mg/mL) aqueous solution. The molar ratio of BSA/NGd is 1:2. The resultant mixture was stirred for 30 min at room temperature. Under a stirring at 400 rpm, additional THF was added dropwise to the above mixture until the solution became slightly turbid. Then 100 μL of 2.5% glutaraldehyde aqueous solution was added, and the reaction was covered with aluminum foils and stirring at room temperature for 4 h. Afterward, the mixture was concentrated in vacuum to remove organic solutions at room temperature. And the NGd-AAs were purified three times by ultrafiltration with Amicon centrifuge tubes (MWCO = 30 kDa) and redispersion in DI-water under sonication. The Gd(III) concentration was measured byinductively coupled plasma atomic emission spectroscopy (ICP-AES). The encapsulation efficiency (EE) of NGd was calculated according to the following eq 1.

$$\mathrm{EE} = \frac{\text{mass of encapsulated NGd}}{\text{total mass of added NGd}} \times 100\% \quad (1)$$

ASSOCIATED CONTENT

Supporting Information

The Supporting Information is available free of charge at https://pubs.acs.org/doi/10.1021/acsnano.1c01251.

Experimental methods, ^{1}H and ^{13}C NMR spectra of intermediate compound and NGd, the curves of r_1 relaxivity and MTT (PDF)

AUTHOR INFORMATION

Corresponding Authors

Zhiming Wang − *State Key Laboratory of Luminescent Materials and Devices, Guangdong Provincial Key Laboratory of Luminescence from Molecular Aggregates, AIE Institute, Center for Aggregation-Induced Emission, South China University of Technology, Guangzhou 510640, China;* orcid.org/0000-0002-3047-3285; Email: wangzhiming@scut.edu.cn

Anjun Qin − *State Key Laboratory of Luminescent Materials and Devices, Guangdong Provincial Key Laboratory of Luminescence from Molecular Aggregates, AIE Institute, Center for Aggregation-Induced Emission, South China University of Technology, Guangzhou 510640, China;* orcid.org/0000-0001-7158-1808; Email: msqinaj@scut.edu.cn

Authors

Lirong Wang − *State Key Laboratory of Luminescent Materials and Devices, Guangdong Provincial Key Laboratory of Luminescence from Molecular Aggregates, AIE Institute, Center for Aggregation-Induced Emission, South China University of Technology, Guangzhou 510640, China*

Qing Wan − *State Key Laboratory of Luminescent Materials and Devices, Guangdong Provincial Key Laboratory of Luminescence from Molecular Aggregates, AIE Institute, Center for Aggregation-Induced Emission, South China University of Technology, Guangzhou 510640, China*

Rongyuan Zhang − *Department of Urology, The First Affiliated Hospital of Soochow University, Suzhou 215006, China*

Bo Situ − *Department of Laboratory Medicine, Nanfang Hospital, Southern Medical University, Guangzhou 510515, China*

Kaiyuan Ni − *Koch Institute for Integrative Cancer Research, Massachusetts Institute of Technology, Cambridge, Massachusetts 02142, United States*

Jinhao Gao − *Department of Chemical Biology, College of Chemistry and Chemical Engineering, Xiamen University, Xiamen 361005, China;* orcid.org/0000-0003-3215-7013

Xing Feng − *School of Material and Energy, Guangdong University of Technology, Guangzhou 510006, China;* orcid.org/0000-0002-4273-979X

Pengfei Zhang − *Guangdong Key Laboratory of Nanomedicine, Shenzhen Engineering Laboratory of Nanomedicine and Nanoformulations, CAS Key Laboratory of Health Informatics, Institute of Biomedicine and Biotechnology, Shenzhen Institute of Advanced Technology, Chinese Academy of Sciences, Shenzhen 518055, China;* orcid.org/0000-0003-0390-3806

Ben Zhong Tang − *State Key Laboratory of Luminescent Materials and Devices, Guangdong Provincial Key Laboratory of Luminescence from Molecular Aggregates, AIE Institute, Center for Aggregation-Induced Emission, South China University of Technology, Guangzhou 510640, China; Shenzhen Institute of Molecular Aggregate Science and Engineering, School of Science and Engineering, The Chinese University of Hong Kong, Shenzhen City, Guangdong 518172, China;* orcid.org/0000-0002-0293-964X

Complete contact information is available at: https://pubs.acs.org/10.1021/acsnano.1c01251

Author Contributions

L.W. conducted the experiments and prepared the manuscript. Q.W. provided the NGd compound. R.Z. provided the assistant to CLSM. B.S. provided the serological test. K.N. helped modify the manuscript. J.G. provided the MRI measurement at 0.5 T. X.F. provided the *in vivo* MRI measurement at 1 T. P.Z. provided the *in vivo* FLI. Z.W., A.Q., and B.Z.T. supervised the experiments and the preparation of manuscript.

Author Contributions

●These authors contributed equally.

Notes

The authors declare no competing financial interest.

ACKNOWLEDGMENTS

This work was financially supported by the National Natural Science Foundation of China (21788102, 21525417, and 51620105009), the Natural Science Foundation of Guangdong Province (2019B030301003, 2019A1515012144, and 2016A030312002), the National Key Research and Development Program of China (Intergovernmental cooperation project, 2017YFE0132200), and the Innovation and Technology Commission of Hong Kong (ITC−CNERC14S01). This work has been submitted to ChemRxiv as a preprint: Lirong Wang, Qing Wang, Rongyuan Zhang, Bo Situ, Kaiyuan Ni, Jinhao Gao, Zhiming Wang, Anjun Qin, Ben Zhong Tang, Synergetic Enhancement of Fluorescence and Magnetic Resonance Signals Assisted by Albumin Cage. 2020, ChemRxiv. DOI: 10.26434/chemrxiv.13123034.v1, URL: https://chemrxiv.org/articles/preprint/Synergetic_Enhancement_of_Fluorescence_and_Magnetic_Resonance_Signals_Assisted_by_Albumin_Cage/13123034 (accessed Oct. 22, 2020).

REFERENCES

(1) Bray, F.; Ferlay, J.; Soerjomataram, I.; Siegel, R. L.; Torre, L. A.; Jemal, A. Global Cancer Statistics 2018: GLOBOCAN Estimates of Incidence and Mortality Worldwide for 36 Cancers in 185 Countries. *Ca-Cancer J. Clin.* **2018**, *68*, 394−424.

(2) James, M. L.; Gambhir, S. S. A Molecular Imaging Primer: Modalities, Imaging Agents, and Applications. *Physiol. Rev.* **2012**, *92*, 897−965.

(3) Karaman, D. S.; Sarparanta, M. P.; Rosenholm, J. M.; Airaksinen, A. J. Multimodality Imaging of Silica and Silicon Materials *in Vivo*. *Adv. Mater.* **2018**, *30*, No. e1703651.

(4) Talanov, V. S.; Regino, C. A.; Kobayashi, H.; Bernardo, M.; Choyke, P. L.; Brechbiel, M. W. Dendrimer-Based Nanoprobe for Dual Modality Magnetic Resonance and Fluorescence Imaging. *Nano Lett.* **2006**, *6*, 1459−1463.

(5) Yan, R.; Hu, Y.; Liu, F.; Wei, S.; Fang, D.; Shuhendler, A. J.; Liu, H.; Chen, H. Y.; Ye, D. Activatable NIR Fluorescence/MRI Dual-Modal Probes for *in Vivo* Imaging by Enzyme-Mediated Fluorogenic Reaction and Self-Assembly. *J. Am. Chem. Soc.* **2019**, *141*, 10331−10341.

(6) Rivas, C.; Stasiuk, G. J.; Gallo, J.; Minuzzi, F.; Rutter, G. A.; Long, N. J. Lanthanide(III) Complexes of Rhodamine-DO3A Conjugates as Agents for Dual-Modal Imaging. *Inorg. Chem.* **2013**, *52*, 14284−14293.

(7) Harrison, V. S.; Carney, C. E.; MacRenaris, K. W.; Waters, E. A.; Meade, T. J. Multimeric Near IR-MR Contrast Agent for Multimodal *in Vivo* Imaging. *J. Am. Chem. Soc.* **2015**, *137*, 9108−9116.

(8) Li, H.; Parigi, G.; Luchinat, C.; Meade, T. J. Dual-Modal Fluorescence-Magnetic Resonance Contrast Agent for Apoptosis Imaging. *J. Am. Chem. Soc.* **2019**, *141*, 6224−6233.

(9) Wahsner, J.; Gale, E. M.; Rodriguez-Rodriguez, A.; Caravan, P. Chemistry of MRI Contrast Agents: Current Challenges and New Frontiers. *Chem. Rev.* **2019**, *119*, 957−1057.

(10) Ananta, J. S.; Godin, B.; Sethi, R.; Moriggi, L.; Liu, X.; Serda, R. E.; Krishnamurthy, R.; Muthupillai, R.; Bolskar, R. D.; Helm, L.; Ferrari, M.; Wilson, L. J.; Decuzzi, P. Geometrical Confinement of Gadolinium-Based Contrast Agents in Nanoporous Particles Enhances T1 Contrast. *Nat. Nanotechnol.* **2010**, *5*, 815−821.

(11) Gizzatov, A.; Stigliano, C.; Ananta, J. S.; Sethi, R.; Xu, R.; Guven, A.; Ramirez, M.; Shen, H.; Sood, A.; Ferrari, M.; Wilson, L. J.; Liu, X.; Decuzzi, P. Geometrical Confinement of Gd(DOTA) Molecules within Mesoporous Silicon Nanoconstructs for MR Imaging of Cancer. *Cancer Lett.* **2014**, *352*, 97−101.

(12) Ni, K.; Zhao, Z.; Zhang, Z.; Zhou, Z.; Yang, L.; Wang, L.; Ai, H.; Gao, J. Geometrically Confined Ultrasmall Gadolinium Oxide Nanoparticles Boost the T(1) Contrast Ability. *Nanoscale* **2016**, *8*, 3768−3774.

(13) Wang, L.; Lin, H.; Ma, L.; Jin, J.; Shen, T.; Wei, R.; Wang, X.; Ai, H.; Chen, Z.; Gao, J. Albumin-Based Nanoparticles Loaded with Hydrophobic Gadolinium Chelates as T1-T2 Dual-Mode Contrast Agents for Accurate Liver Tumor Imaging. *Nanoscale* **2017**, *9*, 4516−4523.

(14) Hu, J.; Liu, S. Recent Advances on Stimuli-Responsive Macromolecular Magnetic Resonance Imaging (MRI) Contrast Agents. *Sci. China. Chem.* **2018**, *61*, 1110−1122.

(15) Wang, D.; Tang, B. Z. Aggregation-Induced Emission Luminogens for Activity-Based Sensing. *Acc. Chem. Res.* **2019**, *52*, 2559−2570.

(16) Zhang, H.; Liu, J.; Du, L.; Ma, C.; Leung, N. L. C.; Niu, Y.; Qin, A.; Sun, J.; Peng, Q.; Sung, H. H. Y.; illiams, I. D.; Kwok, R. T. K.; Lam, J. W. Y.; Wong, K. S.; Phillips, D. L.; Tang, B. Z. Drawing a Clear Mechanistic Picture for the Aggregation-Induced Emission Process. *Mater. Chem. Front.* **2019**, *3*, 1143−1150.

(17) Cai, X.; Liu, B. Aggregation-Induced Emission: Recent Advances in Materials and Biomedical Applications. *Angew. Chem., Int. Ed.* **2020**, *59*, 9868−9886.

(18) Li, J.; Wang, J.; Li, H.; Song, N.; Wang, D.; Tang, B. Z. Supramolecular Materials Based on AIE Luminogens (AIEgens): Construction and Applications. *Chem. Soc. Rev.* **2020**, *49*, 1144−1172.

(19) Chen, Y.; Li, M.; Hong, Y.; Lam, J. W.; Zheng, Q.; Tang, B. Z. Dual-Modal MRI Contrast Agent with Aggregation-Induced Emission Characteristic for Liver Specific Imaging with Long Circulation Lifetime. *ACS Appl. Mater. Interfaces* **2014**, *6*, 10783−10791.

(20) Kratz, F. Albumin as a Drug Carrier: Design of Prodrugs, Drug Conjugates and Nanoparticles. *J. Controlled Release* **2008**, *132*, 171−183.

(21) Sleep, D.; Cameron, J.; Evans, L. R. Albumin as a Versatile Platform for Drug Half-Life Extension. *Biochim. Biophys. Acta, Gen. Subj.* **2013**, *1830*, 5526−5534.

(22) Liu, Z.; Chen, X. Simple Bioconjugate Chemistry Serves Great Clinical Avances: Albumin as a Versatile Platform for Diagnosis and Precision Therapy. *Chem. Soc. Rev.* **2016**, *45*, 1432−1456.
(23) Liu, X.; Wang, C.; Liu, Z. Protein-Engineered Biomaterials for Cancer Theranostics. *Adv. Healthcare Mater.* **2018**, *7*, No. e1800913.
(24) Caravan, P. Protein-Targeted Gadolinium-Based Magnetic Resonance Imaging (MRI) Contrast Agents: Design and Mechanism of Action. *Acc. Chem. Res.* **2009**, *42*, 851−862.
(25) Boros, E.; Caravan, P. Structure-Relaxivity Relationships of Serum Albumin Targeted MRI Probes Based on a Single Amino Acid Gd Complex. *J. Med. Chem.* **2013**, *56*, 1782−1786.
(26) Gao, S.; Wei, G.; Zhang, S.; Zheng, B.; Xu, J.; Chen, G.; Li, M.; Song, S.; Fu, W.; Xiao, Z.; Lu, W. Albumin Tailoring Fluorescence and Photothermal Conversion Effect of Near-Infrared-II Fluorophore with Aggregation-Induced Emission Characteristics. *Nat. Commun.* **2019**, *10*, 2206.
(27) Wang, S.; Hu, F.; Pan, Y.; Ng, L. G.; Liu, B. Bright AIEgen-Protein Hybrid Nanocomposite for Deep and High-Resolution *in Vivo* Two Photon Brain Imaging. *Adv. Funct. Mater.* **2019**, *29*, 1902717.
(28) He, T.; Niu, N.; Chen, Z.; Li, S.; Liu, S.; Li, J. Novel Quercetin Aggregation-Induced Emission Luminogen (AIEgen) with Excited-State Intramolecular Proton Transfer for *in Vivo* Bioimaging. *Adv. Funct. Mater.* **2018**, *28*, 1706196.
(29) Esqueda, A. C.; Lopez, J. A.; Andreu-De-Riquer, G.; Alvarado-Monzon, J. C.; Ratnakar, J.; Lubag, A. J.; Sherry, A. D.; De Leon-Rodriguez, L. M. A New Gadolinium-Based MRI Zinc Sensor. *J. Am. Chem. Soc.* **2009**, *131*, 11387−11391.
(30) Zhou, Z.; Wang, L.; Chi, X.; Bao, J.; Yang, L.; Zhao, W.; Chen, Z.; Wang, X.; Chen, X.; Gao, J. Engineered Iron-Oxide-Based Nanoparticles as Enhanced T1 Contrast Agents for Efficient Tumor Imaging. *ACS Nano* **2013**, *7*, 3287−3296.
(31) Wang, L.; Lin, H.; Chi, X.; Sun, C.; Huang, J.; Tang, X.; Chen, H.; Luo, X.; Yin, Z.; Gao, J. A Self-Assembled Biocompatible Nanoplatform for Multimodal MR/Fluorescence Imaging Assisted Photothermal Therapy and Prognosis Analysis. *Small* **2018**, *14*, No. e1801612.
(32) Zhou, Z.; Huang, D.; Bao, J.; Chen, Q.; Liu, G.; Chen, Z.; Chen, X.; Gao, J. A Synergistically Enhanced T(1) -T(2) Dual-Modal Contrast Agent. *Adv. Mater.* **2012**, *24*, 6223−6228.
(33) Greish, K. Enhanced Permeability and Retention (EPR) Effect for Anticancer Nanomedicine Drug Targeting. *Methods Mol. Biol.* **2010**, *624*, 25−37.
(34) Kang, H.; Rho, S.; Stiles, W. R.; Hu, S.; Baek, Y.; Hwang, D. W.; Kashiwagi, S.; Kim, M. S.; Choi, H. S. Size-Dependent EPR Effect of Polymeric Nanoparticles on Tumor Targeting. *Adv. Healthcare Mater.* **2020**, *9*, No. e1901223.
(35) Yang, K.; Wan, J.; Zhang, S.; Zhang, Y.; Lee, S. T.; Liu, Z. *In Vivo* Pharmacokinetics, Long-Term Biodistribution, and Toxicology of PEGylated Graphene in Mice. *ACS Nano* **2011**, *5*, 516−522.
(36) Sharma, N.; Saifi, M. A.; Singh, S. B.; Godugu, C. *In Vivo* Studies: Toxicity and Biodistribution of Nanocarriers in Organisms. *In Nanotoxicity* **2020**, 41−70.
(37) Longmire, M.; Choyke, P.; Kobayashi, H. Clearance Properties of Nano-Sized Particles and Molecules as Imaging Agents: Considerations and Caveats. *Nanomedicine* **2008**, *35*, 703−717.
(38) Wei, P.; Duan, L.; Zhang, D.; Qiao, J.; Wang, L.; Wang, R.; Dong, G.; Qiu, Y. A New Type of Light-Emitting Naphtho[2,3-c][1,2,5]-thiadiazole Derivatives: Synthesis, Photophysical Characterization and Transporting Properties. *J. Mater. Chem.* **2008**, *18*, 806−818.
(39) Yen, Y. S.; Ni, J. S.; Hung, W. I.; Hsu, C. Y.; Chou, H. H.; Lin, J. T. Naphtho[2,3-c][1,2,5]thiadiazole and 2H-Naphtho[2,3-d][1,2,3]-triazole-Containing D-A-pi-A Conjugated Organic Dyes for Dye-Sensitized Solar Cells. *ACS Appl. Mater. Interfaces* **2016**, *8*, 6117−6126.
(40) Jun, J. Y.; Nguyen, H. H.; Paik, S.-Y.-R.; Chun, H. S.; Kang, B.-C.; Ko, S. Preparation of Size-Controlled Bovine Serum Albumin (BSA) Nanoparticles by a Modified Desolvation Method. *Food Chem.* **2011**, *127*, 1892−1898.

https://doi.org/10.1021/acsnano.1c01251
ACS Nano 2021, 15, 9924−9934